photonics

MDPI

Article

Two-Dimensional Quasi-Periodic Diffraction Properties of the Scalar and Vector Optical Fields

Yue Pan *, Xue-Feng Sun, Guang-Bo Zhang, Qing-Lu Li, Ya-Ning Kong, Tian-Fei Zhao and Xu-Zhen Gao

School of Physics and Physical Engineering, Shandong Provincial Key Laboratory of Laser Polarization and Information Technology, Qufu Normal University, Qufu 273165, China; xzhgao@qfnu.edu.cn (X.-Z.G.)
* Correspondence: panyue.89@163.com or panyue@qfnu.edu.cn

Abstract: As is known, quasi-periodicity attracts great attention in many scientific regions. For instance, the discovery of the quasicrystal was rewarded the Nobel Prize in 2011, leading to a series of its applications. However, in the area of manipulating optical fields, the two-dimensional quasi-periodicity is rarely considered. Here, we study the two-dimensional quasi-periodic diffraction properties of the scalar and vector optical fields based on the Penrose tiling, which is one of the most representative kinds of two-dimensional quasi-periodic patterns. We propose type-A and type-B Penrose tiling masks (PTMs) with phase modulation, and further show the diffraction properties of the optical fields passing through these masks. The intensity of the diffraction field holds a tenfold symmetry. It is proved that the iteration number n of the PTM shows the "weeding" function in the diffraction field, and this property is useful in filtering, shaping, and manipulating diffraction fields. Meanwhile, we also find that the diffraction patterns have the label of the Golden ratio, which can be applied in areas such as optical encryption and information transmission.

Keywords: diffraction; vector beam; quasi-periodicity; structured light

Citation: Pan, Y.; Sun, X.-F.; Zhang, G.-B.; Li, Q.-L.; Kong, Y.-N.; Zhao, T.-F.; Gao, X.-Z. Two-Dimensional Quasi-Periodic Diffraction Properties of the Scalar and Vector Optical Fields. *Photonics* **2023**, *10*, 1045. https://doi.org/10.3390/photonics10091045

Received: 24 August 2023
Revised: 2 September 2023
Accepted: 5 September 2023
Published: 14 September 2023

1. Introduction

As is known, quasi-periodicity attracts great attention and has been applied in many scientific regions. For instance, the discovery of the quasicrystal attracted great interest and changed the perception of the crystal. Before 1981, the existence of the quasicrystal was considered as unrealistic because of their forbidden fivefold and tenfold symmetries. In 1982, Daniel Shechtman found a material called a quasicrystal that possesses long-range order without translational periodicity [1], which was awarded the Nobel Prize in 2011. After 1982, the quasicrystal has attracted wide attention, and its corresponding quasi-periodic model gradually developed. According to dimensions, quasi-periodic models can be divided into one-dimensional quasi-periodic models, two-dimensional quasi-periodic models, and three-dimensional quasi-periodic models. Quasi-periodic models are used not only in the field of materials, but also in the field of optics. One-dimensional quasi-periodic structures have attracted people's attention in the field of diffraction optics. It has been applied in designing quasi-periodic masks including Fibonacci gratings [2–6], Fibonacci zone plate [7,8], and Fibonacci-like zone plate [9]. These masks can be used for different applications, such as super-resolution imaging [5,6,10,11], intraocular lenses [8,9,12], biomedical imaging [11], and filtering [13]. Compared to the one-dimensional quasi-periodic structures, the two-dimensional quasi-periodic structures possess more variations, which can be more flexible when designing and manipulating optical fields. However, the two-dimensional quasi-periodic structures are rarely considered in manipulating optical fields, which can be meaningful in optical research.

Polarization is one of the most salient features of light, even more important than the coherence property. During the past few years, manipulation of polarization has become an appealing and promising topic in the area of physical optics. Polarization, as an

additional degree of freedom, is used in creating the vector optical field (VOF) with a spatially inhomogeneous state of polarization [14,15]. Compared with the scalar optical field (SOF) with a uniform polarization distribution, VOFs with space-variant polarization structures have attracted extensive interest due to many unique features [16–21]. VOFs hold great potential for a variety of scientific and engineering applications, such as optical communications [17,22], far-field focal spot beyond the diffraction limit [23], focal engineering [24–27] , optical microscopy [28,29], light–matter interactions [30,31], and quantum entanglement [32]. Thus, it is of significance to study the two-dimensional quasi-periodic diffraction properties of both SOF and VOF, which may lead to new properties and applications.

In this paper, we study the two-dimensional quasi-periodic diffraction properties of the optical fields based on the Penrose tiling, which is one of the most representative quasi-periodic patterns. We propose two different kinds of Penrose tiling masks (PTMs). Type-A PTM is a kind of phase PTM with different phases in different rhombus tiles, and type-B PTM contains circular tiles to modulate phase distribution. Based on these two kinds of PTMs, we study the diffraction properties of the SOF with a homogeneous polarization state and the VOF with a space-variant polarization state, respectively. As a result, the diffraction patterns show a tenfold symmetry. In the diffraction field, the iteration number n of the Penrose tiling possesses the "weeding" function, as the noise spots around the strong spot become weaker when the iteration number increases. Moreover, the diffraction pattern of the optical field passing through the PTM shows the label of the Golden ratio, which can be a featured and characteristic mark of the diffraction field. These results are inspirable and useful in areas such as manipulating and shaping diffraction fields, optical encryption, and information transmission.

2. The Design of Penrose Tiling Masks and Basic Diffraction Properties

The Penrose tiling, which is one of the most representative kinds of two-dimensional quasi-periodic structures, was first proposed by Penrose [33,34]. The Penrose tiling is used not only in quasicrystal models of crystallography, but also in various branches such as nature, art, materials and so on. Here, we consider the most common rhombic Penrose tiling which is built up by fat rhombus tiles and thin rhombus tiles. The rhombic Penrose tiling can be generated by the Penrose substitution rule [35–37], which means that it is designed by taking a tile, expanding it, and then replacing the larger tiles by copies of the original tiles. The tiles in the Penrose tiling are always replaced in the same way. Obviously, this is an iteration process [35,37], and the number of iterations is n. Based on the rhombic Penrose tiling, we propose type-A and type-B PTMs with phase modulation when $n = 3$, as shown in Figure 1a and Figure 1b, respectively. For type-A PTM, the phase is modulated to zero and π in the fat rhombus tiles and thin rhombus tiles, respectively. Type-A PTM is exactly with fivefold symmetry, and the acute angles of fat rhombus tiles and thin rhombus tiles are 72° and 36°, respectively. Considering the strong diffraction effect of the rhombic mask, we further propose type-B PTM, as shown in Figure 1b. In this kind of PTM, the circle tiles are applied instead of the rhombus tiles, and the phases are modulated to zero and π in two different circle tiles in type-B PTM.

Based on the Fraunhofer diffraction, we explore the diffraction properties of the optical fields through the two kinds of PTMs. The Fraunhofer diffraction formula is [38,39]

$$\begin{bmatrix} E'_x(x',y') \\ E'_y(x',y') \end{bmatrix} = \frac{1}{i\lambda z} e^{i\frac{k}{2z}(x'^2+y'^2)} \iint \begin{bmatrix} E_x(x,y) \\ E_y(x,y) \end{bmatrix} e^{-i\frac{2\pi}{\lambda z}(xx'+yy')} P(x,y)dxdy, \quad (1)$$

where (x', y') are the coordinates in the diffraction plane, while (x, y) are the coordinates in the input plane. z is the longitudinal coordinate. $k = 2\pi/\lambda$ is the wavenumber, and λ is the wavelength of light. $P(x, y)$ is the aperture function of the input field. In the experiment, we use the focal field to study the far-field diffraction field, and the calculation formula is [40–42]

$$\begin{bmatrix} E_{x_f}(x_f, y_f) \\ E_{y_f}(x_f, y_f) \end{bmatrix} = \frac{1}{i\lambda f} e^{i\frac{k}{2f}(x_f + y_f)} \iint \begin{bmatrix} E_x(x,y) \\ E_y(x,y) \end{bmatrix} e^{-i\frac{2\pi}{\lambda f}(xx_f + yy_f)} \operatorname{circ}\left[\frac{\sqrt{x^2+y^2}}{f\mathrm{NA}}\right] dxdy, \quad (2)$$

where (x_f, y_f) are the coordinates in the focal plane, and f is the focal length of the lens. circ$(\cdot)$ is the well-known circular function describing the boundary of the input field. The numerical aperture of the focal lens is NA $= \rho_m / f$, where ρ_m is the maximum radius of the input field. We choose NA $= 0.02$ in the following calculation.

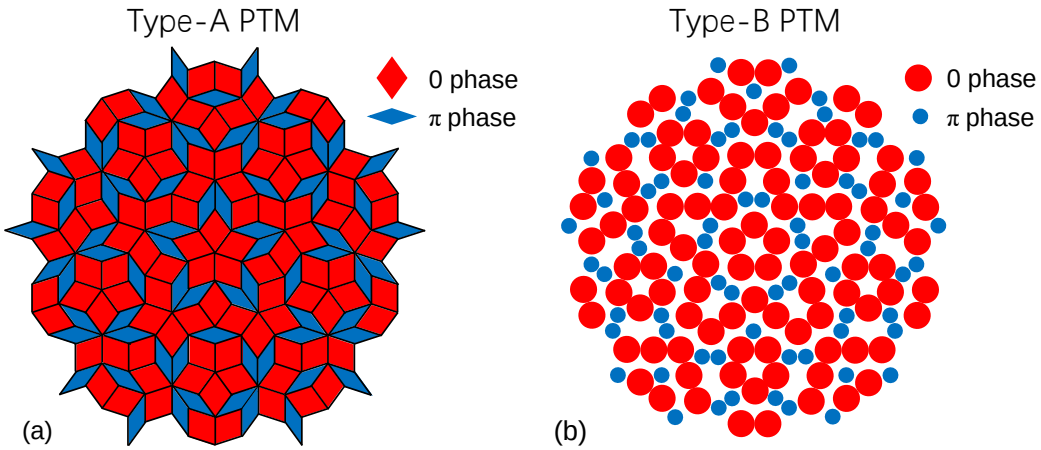

Figure 1. Two kinds of PTMs when the iteration number $n = 3$. (**a**) Type-A PTM with rhombic tiles. (**b**) Type-B PTM with circular tiles. Phases 0 and π are modulated in different tiles in the PTMs.

Next, we study the diffraction properties of the SOF with uniform polarization distribution and the VOF with space-variant polarization distribution through the PTMs. For simplicity, we choose the x-polarized SOF as $\mathbf{E} = \hat{\mathbf{e}}_x$, which means $E_x(x,y) = 1$ and $E_y(x,y) = 0$ in Equations (1) and (2). For the input VOF, we choose the most common cylindrical VOF as $\mathbf{E} = \cos(m\varphi)\hat{\mathbf{e}}_x + \sin(m\varphi)\hat{\mathbf{e}}_y$, so $E_x(x,y) = \cos(m\varphi)$ and $E_y(x,y) = \sin(m\varphi)$ in Equations (1) and (2). Here, φ is the azimuthal coordinate in the input plane, and m is the topological charge of the cylindrical VOF. When $m = 1$, the cylindrical VOF degrades into the radially polarized field, whose linear polarizations in the wave front are along the radial direction. As is known, though there are various kinds of VOFs, the radially polarized VOF is the most common VOF, which has been applied in many areas [14,15,17,20–22,24–26,29,30,32]. This is the reason why we mainly focus on studying the radially polarized VOF here.

Figure 2 shows the diffraction patterns of the x-polarized SOF passing through type-A and type-B PTMs with $n = 4$. When type-A PTM is applied, the diffraction pattern exhibits one strong focal spot at the center, as shown in the first row of Figure 2. In order to show more details of the diffraction patterns, we magnify the intensity of the diffraction patterns to different degrees. When the intensity is magnified 20 and 50 times, more diffraction spots appear around the central spot, but the diffraction patterns always exhibit a tenfold mirror symmetry. When type-B PTM is applied, the diffraction pattern also exhibits one strong focal spot at the center and a tenfold mirror symmetry, as shown in the second row of Figure 2. Compared with the case of type-A PTM, the size of the diffraction pattern of type-B PTM is smaller. This is easy to understand as the shape of the tiles in type-B PTM is circular, and their diffraction effect is weaker than that of the rhombic tiles in type-A PTM. Meanwhile, the intensity of the secondary diffraction spots is stronger for the case of type-B PTM, as shown in the second and third columns of Figure 2. The number of diffraction spots is smaller for the case of type-B PTM, which can be seen from the fourth column of Figure 2.

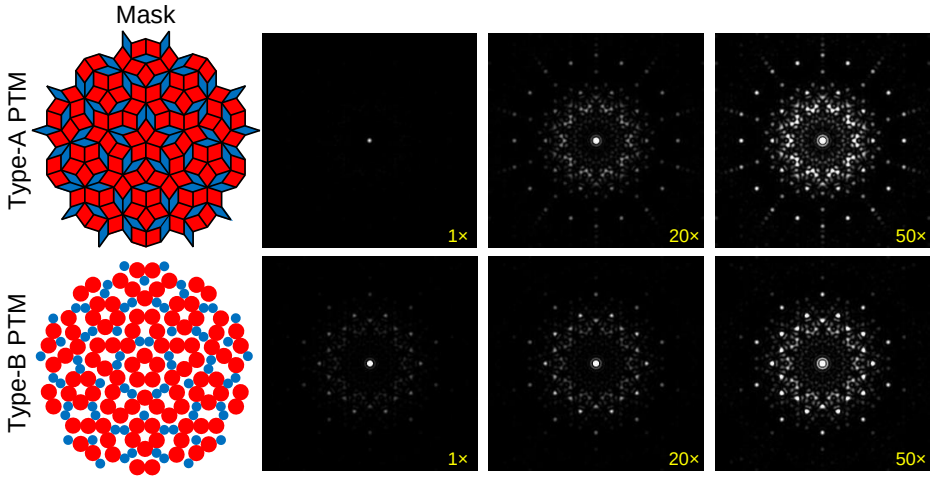

Figure 2. The diffraction patterns of the x-polarized SOFs passing through type-A and type-B PTMs when $n = 4$. The first column shows the schematic of the two kinds of PTMs, and the second to fourth columns show the diffraction patterns when the intensity is magnified 1, 20, and 50 times, respectively. Any image of the diffraction field has a dimension of $2000\lambda \times 2000\lambda$.

Figure 3 shows the diffraction patterns of the VOFs when $m = 1$ and 2 passing through type-A and type-B PTMs, respectively. Obviously, the diffraction spots in the intensity patterns are also with space-variant polarizations, and the topological charge of each focal ring is the same with the incident VOF. When we observe the x component of the diffraction field in the second column of Figure 3, any diffraction ring exhibits two petals, which is two times the topological charge m of the incident VOF. Meanwhile, the diffraction spot exhibits four petals when $m = 2$ in the fourth column of Figure 3, and the number of the petals is also two times that of m. All the diffraction patterns exhibit a tenfold mirror symmetry, and the diffraction patterns when $m = 2$ are extremely similar to the patterns when $m = 1$, except that the size of the focal ring when $m = 2$ is larger. We should also point out that we only showed the total intensity and the intensity of the x component in Figure 3, and the intensity of the y component can be derived by the total intensity and the intensity of the x component.

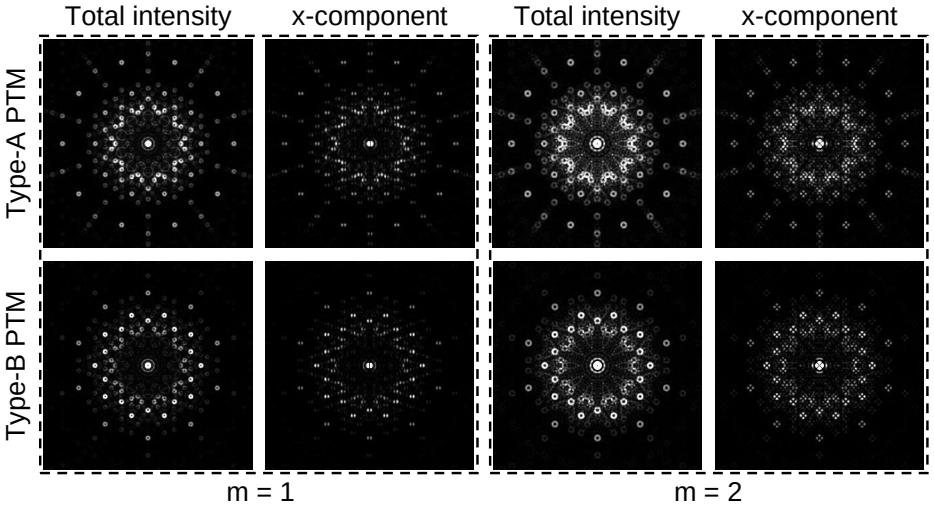

Figure 3. The diffraction patterns of the cylindrical VOFs passing through type-A and type-B PTMs when $n = 5$. The first and second columns show the case of input VOF when $m = 1$, and the third and fourth columns show the case of input VOF when $m = 2$. The first and third columns show the total intensity distributions, and the second and fourth columns show the intensity distributions of the x components, respectively. The intensity is magnified 30 times in all the images. Any image has a dimension of $3000\lambda \times 3000\lambda$.

3. The "Weeding" Function of the Iteration Number n In PTMs

For the PTMs we propose, there is an important modulation degree of freedom to control and manipulate the diffraction fields. This parameter is the iteration number n of the PTM, which holds the "weeding" function in modulating the diffraction field. The "weeding" function is an important property when modulating and applying the diffraction field or the focal field [39,43]. When the field is weeded, the energies of the diffraction field or the focal field become more concentrated, which can be applied in a variety of areas, including focal engineering, optical trapping, optical machining, and information transmission. Figure 4 shows the diffraction patterns of the x-polarized SOF passing through type-A and type-B PTMs when $n = 3$, 4, and 5 in three rows, respectively. From the first and third columns, we can see that the diffraction patterns always exhibit a tenfold mirror symmetry for all the cases. When n increases, the sizes of the intensity patterns also increase, which is understandable as the complexity of the phase mask increases along with the increasing n. Meanwhile, the sizes of the diffraction patterns are always smaller for the case of type-B PTM. From the enlarged figures in the second and fourth columns, it can be found that the diffraction spots become cleaner with the increasing values of n. This proves the "weeding" function of the iteration number n of type-A and type-B PTMs for the input SOF.

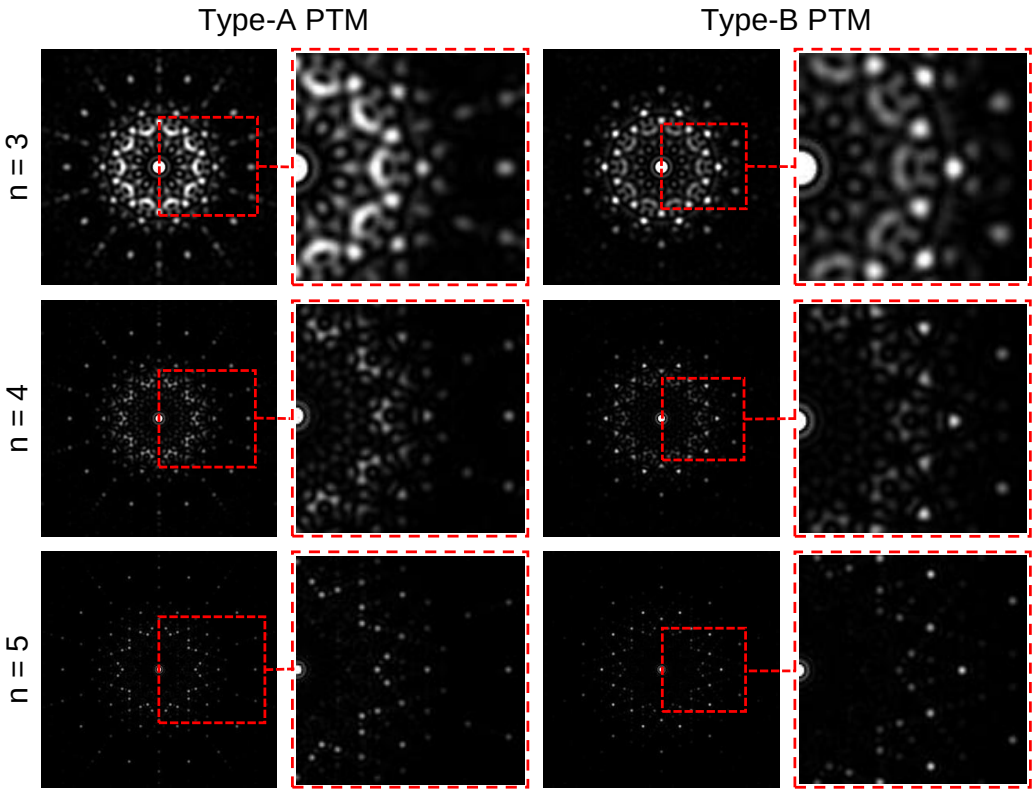

Figure 4. The diffraction patterns of the x-polarized SOF passing through type-A and type-B PTMs when $n = 3$, 4, and 5. The first and second columns show the case of type-A PTM, and the third and fourth rows show the case of type-B PTM, respectively. The three rows show the cases of the PTMs when $n = 3$, 4, and 5, respectively. The intensity is magnified 20 times in all the images. The images in the first and third columns have the dimensions of $1200\lambda \times 1200\lambda$ in the first row, $2000\lambda \times 2000\lambda$ in the second row, and $3000\lambda \times 3000\lambda$ in the third row, respectively.

We discussed the "weeding" function of the iteration number n in the diffraction patterns for the case of input SOF. Now, we further study the case when the input field is VOF. Figure 5 shows the diffraction patterns of the input radially polarized VOF passing through type-A and type-B PTMs when $n = 3$, 4, and 5 in three rows, respectively. The diffraction patterns exhibit a tenfold mirror symmetry in the first and third columns.

When the patterns are enlarged in the second and fourth columns, we can find that the diffraction rings become cleaner with the increasing values of n. This proves that for the case when the input field is VOF, the "weeding" function of the iteration number n of the PTM is also effective. To further discuss the "weeding" function of the iteration number n of the PTM, it is necessary to compare the diffraction fields for the two cases of incident SOF and VOF. By comparing Figures 4 and 5, we can find that with the increasing values of n, the intensity distribution of diffraction fields with the same PTM becomes more and more similar. The difference is that the diffraction field of the SOF is with a series of diffraction spots, while the diffraction field of the VOF is with a series of diffraction rings. From the x components of the diffraction fields, it can be seen that the polarization distribution of the diffraction field is space-variant for the case of incident VOF, and the diffraction fields are with space-invariant polarizations for the case of incident SOF.

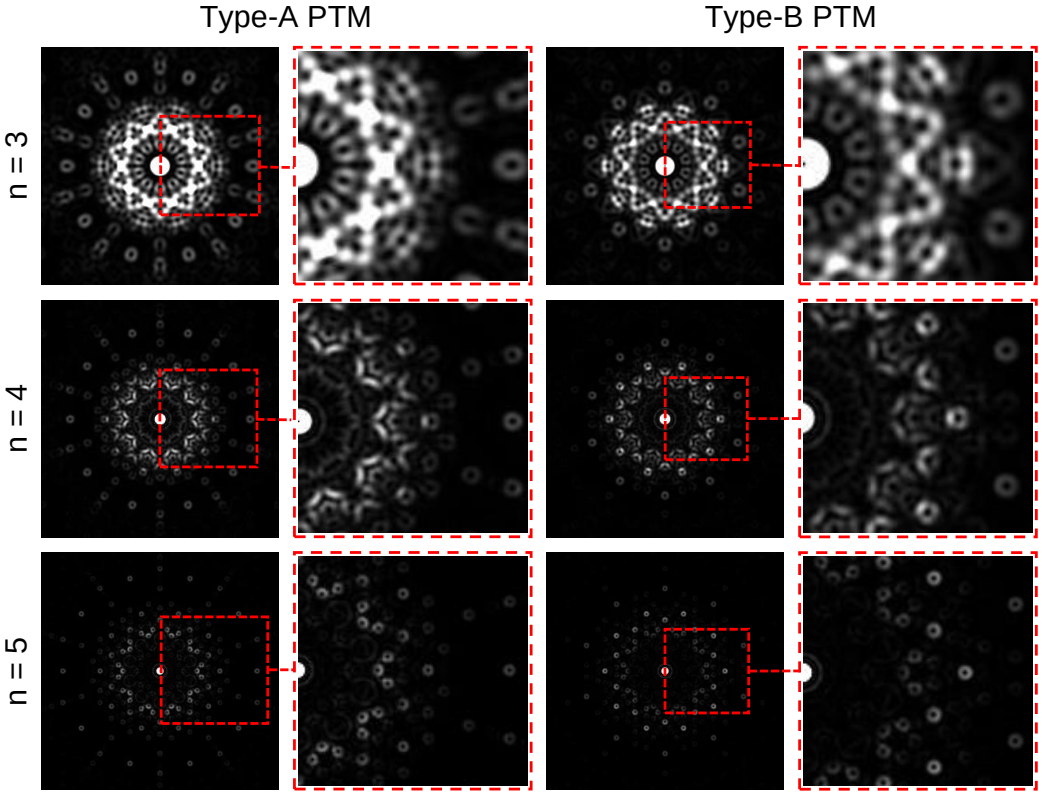

Figure 5. The diffraction patterns of the radially polarized VOF passing through type-A and type-B PTMs when $n = 3$, 4, and 5. The first and second columns show the case of type-A PTM, and the third and fourth columns show the case of type-B PTM, respectively. The three rows show the cases of the PTMs when $n = 3$, 4, and 5, respectively. The intensity is magnified 10 times in all the images. The images in the first and third columns have the dimensions of $1200\lambda \times 1200\lambda$ in the first row, $2000\lambda \times 2000\lambda$ in the second row, and $3000\lambda \times 3000\lambda$ in the third row, respectively.

4. The Label of the Golden Ratio in the Diffraction Patterns

As is known, the quasi-periodicity is closely related to the Golden ratio. For example, the Penrose tiling exhibits multiple instances of the Golden ratio, which is expected due to its fivefold symmetry [36,44,45]. The Golden ratio, also known as the Golden section or Golden number, is an irrational number attracting attention in various subjects. To define the Golden ratio Φ [46–48], a straight-line AB is divided at a point C, and the line AB is divided to a longer line AC and a shorter line CB. Then, we assume that the ratio of the lengths of the two lines AC/CB is equal to the ratio of the sum of the two lines AC + CB to the longer side AC, and this ratio can be called the Golden ratio

$\Phi = \mathrm{AC}/\mathrm{CB} = (\mathrm{AC} + \mathrm{CB})/\mathrm{AC} \approx 1.618$. As is known, the Golden ratio is very common and appears in various areas, including science, art, as well as in nature [46–48].

In this research, we surprisingly find that the Golden ratio also appears in the diffraction patterns of the PTMs. Figure 6 shows the diffraction patterns of the x-polarized SOFs passing through type-A PTMs when $n = 3$, 4, 5, and 6 in four rows. The first column shows the diffraction patterns, and we can see that the diffraction patterns exhibit a tenfold mirror symmetry. The second and third columns offer the enlarged patterns of the blue and red rectangles shown in the first column, and the wavelength λ is used as the normalization of distance. In the enlarged patterns, we choose three peak spots in each pattern, and show the distance between the adjacent diffracting spots. The angles between the connecting lines of these spots and the negative y-axis are 54° and 36°, respectively. We surprisingly find that the distance ratio of the diffraction peak spots in the second and third columns is close to the Golden ratio. This phenomenon can be regarded as the label of the Golden ratio appearing in the diffraction patterns. The labels of the Golden ratio appear 10 times in the diffraction patterns for both cases of PTMs due to the tenfold symmetry of the diffraction patterns. In addition, the case of the diffracted VOF passing through the PTM is similar to the results in Figure 6, except that the diffraction spots become the diffraction rings with space-variant polarization distributions. This means that the label of the Golden ratio also appears in the diffraction pattern of the incident VOF.

Table 1 shows the changing trend of the distance ratio of the blue and red featured diffracting spots in Figure 6 with different n. First of all, we discuss the case of the blue featured spots. The distance ratios of the blue featured spots are 1.543, 1.5718, 1.6083, and 1.6162 when $n = 3$, 4, 5, and 6, respectively. The deviation of these distance ratios with the Golden ratio are 4.63%, 2.86%, 0.6%, and 0.11%, respectively. We can see that when the value of n increases, the distance ratio is gradually closer to the Golden ratio. For the case of the red featured spots, the results are similar. The distance ratios of the red featured spots are 1.3872, 1.537, 1.5783, and 1.5965 when $n = 3$, 4, 5, and 6, respectively. The deviation of these distance ratios with the Golden ratio are 14.26%, 5.01%, 2.45%, and 1.33%, respectively. It can be seen that when choosing the same value of the iteration number n, the distance ratio of blue featured spots is closer to the Golden ratio compared with the case of red featured spots. As n increases, the distance ratio is closer to the Golden ratio for both cases. These results prove that the Golden ratio in the two-dimensional quasi-periodic structure in the input plane can extend to the label of the Golden ratio in the diffraction field. The diffraction pattern with featured diffraction spots carrying the label of the Golden ratio can be applied in various areas. The label of the Golden ratio in the diffraction field can be regarded as a special and characteristic label, which can be used in the areas such as optical encryption and information transmission.

We should point out that we only introduce one configuration of the Penrose tiling in designing the diffraction mask, and other configurations of the Penrose tiling of quasicrystals can also be similarly explored when studying the diffraction properties. In addition to the Penrose tiling, other quasi-periodic models with different symmetries can be selected, such as Ammann–Beenker tiling, Socolar tiling, Bronze mean tiling, random square triangle tiling, rectangle–triangle tiling, and Stampfli–Gähler tiling. With these new kinds of quasi-periodic structures, we can study more quasi-periodic diffraction properties of the optical fields, which may be applied in different areas. We hope that the PTMs we propose can be as useful as the well-known Fibonacci masks, which can be applied in areas such as confocal microscopy, optical micromachining, multiple-plane optical trapping, intraocular lenses, and so on.

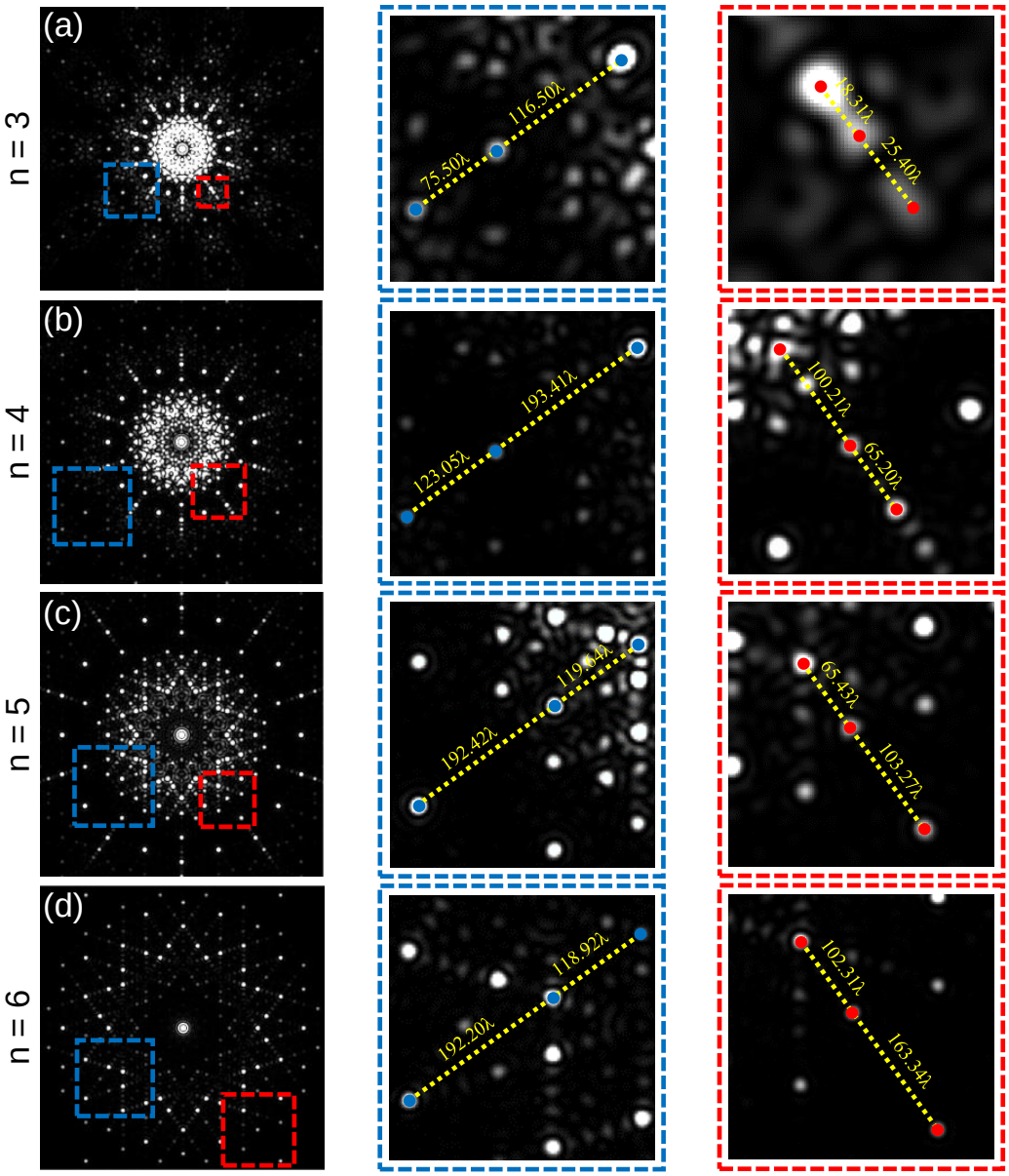

Figure 6. The diffraction patterns of the x-polarized SOFs passing through type-A PTMs when $n = 3$, 4, 5, and 6 in four rows. (**a**–**d**) in the first column show the original diffraction patterns, and the second and third columns show the enlarged patterns of the blue and red rectangles in the first column. The intensity of the diffraction pattern is magnified 150 times. Any image in the first column has a dimension of $2900\lambda \times 2900\lambda$.

Table 1. The distance ratio of featured spots when $n = 3$, 4, 5, and 6.

n	The Distance Ratio of the Blue Featured Spots	Deviation with the Golden Ratio	The Distance Ratio of the Red Featured Spots	Deviation with the Golden Ratio
3	1.5430	4.63%	1.3872	14.26%
4	1.5718	2.86%	1.5370	5.01%
5	1.6083	0.60%	1.5783	2.45%
6	1.6162	0.11%	1.5965	1.33%

Besides the quasi-periodic structures, the kind of the incident optical field is also a very important factor that can influence the diffraction field. In this article, we use the SOF with linear polarization and cylindrical VOFs with $m = 1$ and 2 as the incident optical fields, and the basic diffraction properties are shown and discussed. As we know, there are also other kinds of optical fields that may be applied in studying the two-dimensional quasi-periodic diffraction properties. For the SOF with homogeneous polarization state on the wave front, the SOF with elliptic and circular polarizations can also be used as the incident optical field. As the spin angular momentum (SAM) is associated with circular polarization, the SAM can also be found when the incident field is with elliptic or circular polarizations. For the VOF with space-variant polarizations, there are also many other kinds of VOFs besides the cylindrical VOFs such as hybridly polarized VOF [49,50], full Poincaré sphere VOF [51], fractal VOF [43], and so on. When these different kinds of VOFs are applied in studying the quasi-periodic diffraction properties, the diffraction field with space-variant polarization distribution can be generated, and the symmetry of the diffraction field is decided by the polarization distribution of the incident VOF. We should also point out that besides the SOF and VOF, there is also a kind of vortex optical field with a helical phase of $\exp(-il\varphi)$. The vortex optical field carries the orbital angular momentum (OAM) [52], which can be applied in many regions [53,54]. When the vortex optical field is used in studying the quasi-periodic diffraction properties, the OAM is expected in the diffraction field.

5. Discussion

This research of the two-dimensional quasi-periodic diffraction properties mainly focuses on introducing the two-dimensional quasi-periodicity into the study of the diffraction field. Previous research discussed the cases using the one-dimensional quasi-periodic structures to study the diffraction properties [2–9]. In this article, we choose the two-dimensional quasi-periodic structures to study the diffraction properties, which is novel and inspiring. When the two-dimensional quasi-periodic structures are used as diffraction masks, we find two interesting properties. One is the "weeding" function of the PTMs, as shown in Figures 4 and 5, the other one is the label of the Golden ratio in the diffraction field, as shown in Figure 6 and Table 1. These properties prove that the two-dimensional quasi-periodic structures are useful in studying the diffraction properties. We hope the idea of studying the two-dimensional quasi-periodic diffraction properties can be applied in different areas.

6. Conclusions

In this paper, we propose the quasi-periodic mask to study the diffraction effects, taking the Penrose tiling mask as an example. Type-A and type-B PTMs with a phase modulation of zero and π are proposed. The rhombus tiles are designed in the Penrose tiling for type-A PTM, while the circular tiles are applied in the Penrose tiling for type-B PTM. Based on these two kinds of PTMs, we further study the diffraction properties of SOFs with homogeneous polarization states and VOFs with space-variant polarization states. The diffraction patterns with a tenfold symmetry are achieved. Moreover, the iteration number n of the PTM shows the "weeding" function in the diffraction field, which is useful in filtering, shaping, and manipulating diffraction fields. Meanwhile, the diffraction patterns of the fields passing through the PTMs also have the label of the Golden ratio, as the ratio of the distances of the adjacent featured diffraction spots accords with the Golden ratio. This proves that the characteristic of the Golden ratio can pass from the input field to the diffraction field during the diffraction process. The label of the Golden ratio is an obvious and special feature of the diffraction field passing through the PTM, which can be applied in areas such as optical encryption and information transmission.

Author Contributions: Conceptualization, Y.P. and X.-F.S.; methodology, Y.P. and X.-Z.G.; software, X.-F.S.; validation, Y.P. and X.-F.S.; formal analysis, Y.P., X.-F.S. and G.-B.Z.; investigation, Y.P., X.-F.S., G.-B.Z., Q.-L.L., Y.-N.K. and T.-F.Z.; resources, Y.P. and X.-Z.G.; writing—original draft preparation,

Y.P. and X.-F.S.; writing—review and editing, Y.P., X.-F.S., G.-B.Z. and X.-Z.G.; supervision, Y.P. and X.-Z.G.; funding acquisition, Y.P. and X.-Z.G. All authors have read and agreed to the published version of the manuscript.

Funding: This research was funded by the National Natural Science Foundation of China (11904199), Higher Educational Youth Innovation Science and Technology Program Shandong Province (2022KJ175), and Natural Science Foundation of Shandong Province (ZR2023MA040).

Institutional Review Board Statement: Not applicable.

Informed Consent Statement: Not applicable.

Data Availability Statement: The data that support the findings of this study are available from the first author and the corresponding author upon reasonable request.

Conflicts of Interest: The authors declare no conflict of interest.

References

1. Shechtman, D.; Blech, I.; Gratias, D.; Cahn, J.W. Metallic phase with long-range orientational order and no translational symmetry. *Phys. Rev. Lett.* **1984**, *53*, 1951. [CrossRef]
2. Gao, N.; Zhang, Y.; Xie, C. Circular Fibonacci gratings. *Appl. Opt.* **2011**, *50*, G142–G148. [CrossRef] [PubMed]
3. Verma, R.; Banerjee, V.; Senthilkumaran, P. Fractal signatures in the aperiodic Fibonacci grating. *Opt. Lett.* **2014**, *39*, 2557–2560. [CrossRef] [PubMed]
4. Zhang, C.; Jiang, Z.; Tan, W.; Ge, R.; Liu, J. Non-near-field sub-diffraction focusing in the visible wavelength range by a Fibonacci subwavelength circular grating. *J. Opt. Soc. Am. A* **2018**, *35*, 1701–1704. [CrossRef] [PubMed]
5. Gupta, S.K.; Sun, Z.; Kwok, H.S.; Srivastava, A.K. Low voltage tunable liquid crystal Fibonacci grating. *Liq. Cryst.* **2020**, *47*, 1162–1169. [CrossRef]
6. Sun, Z.B.; Yuan, Z.N.; Nikita, A.; Kwok, H.S.; Srivastava, A.K. Fast-switchable, high diffraction-efficiency ferroelectric liquid crystal Fibonacci grating. *Opt. Express* **2021**, *29*, 13978–13986. [CrossRef]
7. Xia, T.; Cheng, S.; Tao, S. Two pairs of twin foci with the golden mean generated by a modified Fibonacci zone plate. *J. Opt.* **2019**, *21*, 035602. [CrossRef]
8. Rafighdoost, J.; Zhou, Y.; Li, X.; Yan, S.; Zhou, M.; Yao, B. Azimuthally phase-shifted Fibonacci zone plate. *J. Opt. Soc. Am. B* **2020**, *37*, 3557–3563. [CrossRef]
9. Cheng, S.; Liu, M.; Xia, T.; Tao, S. Fibonacci-like zone plate. *Laser Phys.* **2018**, *28*, 066203. [CrossRef]
10. Wu, K.; Wang, G.P. One-dimensional Fibonacci grating for far-field super-resolution imaging. *Opt. Lett.* **2013**, *38*, 2032–2034. [CrossRef]
11. Wu, K.; Wang, G.P. Two-dimensional Fibonacci grating for far-field super-resolution imaging. *Sci. Rep.* **2016**, *6*, 38651. [CrossRef] [PubMed]
12. Machado, F.; Ferrando, V.; Furlan, W.D.; Monsoriu, J.A. Diffractive m-bonacci lenses. *Opt. Express* **2017**, *25*, 8267–8273. [CrossRef] [PubMed]
13. Gong, Y.; Liu, X.; Wang, L. High-channel-count plasmonic filter with the metal–insulator–metal Fibonacci-sequence gratings. *Opt. Lett.* **2010**, *35*, 285–287. [CrossRef] [PubMed]
14. Zhan, Q. Cylindrical vector beams: From mathematical concepts to applications. *Adv. Opt. Photonics* **2009**, *1*, 1–57. [CrossRef]
15. Forbes, A.; de Oliveira, M.; Dennis, M.R. Structured light. *Nat. Photonics* **2021**, *15*, 253–262. [CrossRef]
16. Bauer, T.; Banzer, P.; Karimi, E.; Orlov, S.; Rubano, A.; Marrucci, L.; Santamato, E.; Boyd, R.W.; Leuchs, G. Observation of optical polarization Möbius strips. *Science* **2015**, *347*, 964–966. [CrossRef]
17. Devlin, R.C.; Ambrosio, A.; Rubin, N.A.; Mueller, J.B.; Capasso, F. Arbitrary spin-to-orbital angular momentum conversion of light. *Science* **2017**, *358*, 896–901. [CrossRef]
18. Larocque, H.; Sugic, D.; Mortimer, D.; Taylor, A.J.; Fickler, R.; Boyd, R.W.; Dennis, M.R.; Karimi, E. Reconstructing the topology of optical polarization knots. *Nat. Phys.* **2018**, *14*, 1079–1082. [CrossRef]
19. Gao, X.Z.; Zhao, J.H.; Wang, M.S.; Liu, J.J.; Zhang, G.B.; Pan, Y. Bipolar-variant spin angular momentum and its evolution in a tight focusing process. *Phys. Rev. A* **2020**, *102*, 063514. [CrossRef]
20. Zhao, J.H.; Pan, Y.; Gao, X.Z.; Ma, R.; Man, Z.X.; Ren, Z.C.; Tu, C.; Li, Y.; Wang, H.T. Five-dimensional Poincaré sphere system for representing azimuthally varying vector optical fields. *Phys. Rev. A* **2022**, *106*, 023506. [CrossRef]
21. Zhang, Z.; Zhao, H.; Wu, S.; Wu, T.; Qiao, X.; Gao, Z.; Agarwal, R.; Longhi, S.; Litchinitser, N.M.; Ge, L.; et al. Spin–orbit microlaser emitting in a four-dimensional Hilbert space. *Nature* **2022**, *612*, 246–251. [CrossRef] [PubMed]
22. Sakamoto, M.; Kaneko, Y.; Nakamoto, Y.; Noda, K.; Sasaki, T.; Kawatsuki, N.; Ono, H. Mode demultiplexing of vector beams using crossed-fork-shaped polarization grating fabricated by photoalignment of photo-crosslinkable liquid crystal polymer. *Appl. Phys. Lett.* **2019**, *115*, 061104. [CrossRef]
23. Dorn, R.; Quabis, S.; Leuchs, G. Sharper focus for a radially polarized light beam. *Phys. Rev. Lett.* **2003**, *91*, 233901. [CrossRef] [PubMed]

24. Pan, Y.; Li, S.M.; Mao, L.; Kong, L.J.; Li, Y.; Tu, C.; Wang, P.; Wang, H.T. Vector optical fields with polarization distributions similar to electric and magnetic field lines. *Opt. Express* **2013**, *21*, 16200–16209. [CrossRef] [PubMed]
25. Bauer, T.; Orlov, S.; Peschel, U.; Banzer, P.; Leuchs, G. Nanointerferometric amplitude and phase reconstruction of tightly focused vector beams. *Nat. Photonics* **2014**, *8*, 23–27. [CrossRef]
26. Hu, H.; Gan, Q.; Zhan, Q. Generation of a nondiffracting superchiral optical needle for circular dichroism imaging of sparse subdiffraction objects. *Phys. Rev. Lett.* **2019**, *122*, 223901. [CrossRef]
27. Gao, X.Z.; Zhao, P.C.; Sun, X.F.; Yang, F.; Pan, Y.; Li, Y.; Tu, C.; Wang, H.T. Highly purified transversely polarized optical needle generated by the hybridly polarized vector optical field with hyperbolic symmetry. *J. Opt.* **2020**, *22*, 105604. [CrossRef]
28. Vella, A.; Head, S.T.; Brown, T.G.; Alonso, M.A. Simultaneous measurement of multiple parameters of a subwavelength structure based on the weak value formalism. *Phys. Rev. Lett.* **2019**, *122*, 123603. [CrossRef]
29. Du, L.; Yang, A.; Zayats, A.V.; Yuan, X. Deep-subwavelength features of photonic skyrmions in a confined electromagnetic field with orbital angular momentum. *Nat. Phys.* **2019**, *15*, 650–654. [CrossRef]
30. Ji, Z.; Liu, W.; Krylyuk, S.; Fan, X.; Zhang, Z.; Pan, A.; Feng, L.; Davydov, A.; Agarwal, R. Photocurrent detection of the orbital angular momentum of light. *Science* **2020**, *368*, 763–767. [CrossRef]
31. Dorrah, A.H.; Rubin, N.A.; Zaidi, A.; Tamagnone, M.; Capasso, F. Metasurface optics for on-demand polarization transformations along the optical path. *Nat. Photonics* **2021**, *15*, 287–296. [CrossRef]
32. Ndagano, B.; Perez-Garcia, B.; Roux, F.S.; McLaren, M.; Rosales-Guzman, C.; Zhang, Y.; Mouane, O.; Hernandez-Aranda, R.I.; Konrad, T.; Forbes, A. Characterizing quantum channels with non-separable states of classical light. *Nat. Phys.* **2017**, *13*, 397–402. [CrossRef]
33. Penrose, R. The role of aesthetics in pure and applied mathematical research. *Bull. Inst. Math. Appl.* **1974**, *10*, 266–271.
34. Penrose, R. Pentaplexity a class of non-periodic tilings of the plane. *Math. Intell.* **1979**, *2*, 32–37. [CrossRef]
35. Harriss, E.O. On Canonical Substitution Tilings. Ph.D. Thesis, University of London, London, UK, 2004.
36. Peng, B.Y.; Fu, X.J. Configurations of the Penrose Tiling beyond Nearest Neighbors. *Chin. Phys. Lett.* **2015**, *32*, 056101. [CrossRef]
37. Yan, X.; Yan, W.Q.; Liu, L.; Lu, Y. Penrose tiling for visual secret sharing. *Multimed. Tools Appl.* **2020**, *79*, 32693–32710. [CrossRef]
38. Born, M.; Wolf, E. *Principles of Optics*, 7th ed.; Cambridge University Press: Cambridge, UK, 1999; Volume 461, pp. 401–424.
39. Pan, Y.; Gao, X.Z.; Zhang, X.; Zhao, J.H.; Zhao, P.C.; Li, Y.; Tu, C.; Wang, H.T. Diffraction properties and applications of spatially structured optical fields with fractal amplitude masks. *Appl. Opt.* **2019**, *58*, 8631–8637. [CrossRef]
40. Goodman, J.W. *Introduction to Fourier Optics*; Roberts and Company Publishers: Greenwood Village, CO, USA, 2005.
41. Pan, Y.; Gao, X.Z.; Zhang, G.L.; Li, Y.; Tu, C.; Wang, H.T. Spin angular momentum density and transverse energy flow of tightly focused kaleidoscope-structured vector optical fields. *APL Photonics* **2019**, *4*, 096102. [CrossRef]
42. Sun, X.F.; Gao, X.Z.; Zhang, G.B.; Yang, F.; Liu, J.J.; Ma, R.; Man, Z.X.; Pan, Y. The appearance and annihilation of the spin angular momentum for the multi-polar vector optical field in the focal plane. *APL Photonics* **2023**, *8*, 056101. [CrossRef]
43. Pan, Y.; Gao, X.Z.; Cai, M.Q.; Zhang, G.L.; Li, Y.; Tu, C.; Wang, H.T. Fractal vector optical fields. *Opt. Lett.* **2016**, *41*, 3161–3164. [CrossRef]
44. You, J.Q.; Yan, J.R.; Zhong, J.X.; Yan, X.H. Local electronic properties of two-dimensional Penrose tilings: A renormalization-group approach. *Phys. Rev. B* **1992**, *45*, 7690. [CrossRef] [PubMed]
45. Marples, C.R.; Williams, P.M. The Golden Ratio in Nature: A Tour Across Length Scales. *Symmetry* **2022**, *14*, 2059. [CrossRef]
46. Hemenway, P. *Divine Proportion: Φ in Art, Nature, and Science*; Sterling Publishing Company: New York, NY, USA, 2005.
47. Wang, N.; Ma, J.; Jin, D.; Yu, B. A special golden curve in human upper limbs' length proportion: A functional partition which is different from anatomy. *BioMed Res. Int.* **2017**, *2017*, 4158561. [CrossRef] [PubMed]
48. Wang, M.S.; Gao, X.Z.; Zhao, J.H.; Sun, X.F.; Pan, Y.; Xia, Y. Flexibly modulated Poincaré sphere vector optical field in input and focal planes. *Opt. Express* **2021**, *29*, 21071–21083. [CrossRef]
49. Wang, X.L.; Li, Y.; Chen, J.; Guo, C.S.; Ding, J.; Wang, H.T. A new type of vector fields with hybrid states of polarization. *Opt. Express* **2010**, *18*, 10786–10795. [CrossRef]
50. Lerman, G.M.; Stern, L.; Levy, U. Generation and tight focusing of hybridly polarized vector beams. *Opt. Express* **2010**, *18*, 27650–27657. [CrossRef]
51. Beckley, A.M.; Brown, T.G.; Alonso, M.A. Full poincaré beams. *Opt. Express* **2010**, *18*, 10777–10785. [CrossRef]
52. Allen, L.; Beijersbergen, M.W.; Spreeuw, R.; Woerdman, J. Orbital angular momentum of light and the transformation of Laguerre-Gaussian laser modes. *Phys. Rev. A* **1992**, *45*, 8185. [CrossRef]
53. Yao, A.M.; Padgett, M.J. Orbital angular momentum: Origins, behavior and applications. *Adv. Opt. Photonics* **2011**, *3*, 161–204. [CrossRef]
54. Shen, Y.; Wang, X.; Xie, Z.; Min, C.; Fu, X.; Liu, Q.; Gong, M.; Yuan, X. Optical vortices 30 years on: OAM manipulation from topological charge to multiple singularities. *Light. Sci. Appl.* **2019**, *8*, 90. [CrossRef]